Batteries & Supercaps

Research Article
doi.org/10.1002/batt.202300564

Chemistry
Europe
European Chemical
Societies Publishing

www.batteries-supercaps.org

Bimetallic Nanoparticles Embedded in P,N,Br-Codoped Carbon Matrices Derived from Heterometallic-Organophosphine Frameworks as Electrode Materials for Asymmetric Supercapacitors

Abdallah G. Mahmoud,*[a, b] Jéssica V. Nardeli,*[c] Maria João Ferreira,[a] Ana M. Ferraria,[d, e, f] Ana M. Botelho do Rego,[d, e, f] M. Fátima C. Guedes da Silva,[a, f] and Armando J. L. Pombeiro[a]

An unprecedented method has been developed to obtain heterometallic-organophosphine frameworks (HMOPFs) through a solvent-free, three-component mechanochemical process. In a ball mill, mixing copper (I) bromide with zinc (II), nickel (II) or copper (II) acetates, in the presence of (PTA-CH_2-C_6H_4-p-COOH) Br (PTA is 1,3,5-triaza-7-phosphaadamantane) as an organic linker, has produced the corresponding HMOPFs based on Cu^+-Zn^{2+}, Cu^+-Ni^{2+} and Cu^+-Cu^{2+}, respectively. The pyrolysis of HMOPFs resulted in bimetallic nanoparticles of transition metal phosphide and phosphate embedded in multi-P,N,Br-codoped carbon matrices (Cu–M@C). Due to the utilization of an aminophosphine organic linker, this HMOPFs-derived approach typifies an eco-friendly synthesis of carbon confined transition metal phosphides or phosphates. It avoids the common conventional methods that involves phosphorylation using large amounts of additional P sources, which leads to an intensive release of the flammable and poisonous phosphine gas. Also, the presence of Br at the organic linker eliminates the need for using bromine vapours to obtain halogen-doped carbon matrices. The Cu–M@C nanocomposites were tested as negative electrode materials for asymmetric supercapacitors. Electrochemical tests included cyclic voltammetry and galvano-static charge-discharge experiments, which revealed the Cu–Zn@C electrode with a higher potential window as compared to Cu–Ni@C and Cu–Cu@C electrodes, achieving a rate performance of 60% and high coulombic efficiency.

Introduction

The increasing demand for more sustainable and high-performance batteries and asymmetric supercapacitors for electrical energy storage has led to recent extensive research to develop electrode materials using eco-friendly synthetic strategies.[1–3] Transition metal phosphides (TMPs), submetallic alloys with a general formula M_xP_y, have attracted considerable attention as potential electrode materials due to their high specific capacity, superior electrical conductivity and metalloid properties.[4,5] They exhibit superior electrochemical features when compared to metal oxides, sulfides and selenides counterparts, including in the context of pseudocapacitor electrodes.[6] However, the low durability of TMPs has been a significant challenge in their practical application, addressed by developing carbon-confined TMPs (TMPs@C) nanostructures.[7,8] Utilization of metal-organic frameworks (MOFs) as templates to obtain TMPs@C nano-structures has become a robust approach due to several advantages over other strategies, such as better control of the size and shape of TMP nanoparticles (NPs).[8–12] The synthesis of TMPs@C using a MOF-derived strategy can involve the pyrolysis of MOFs followed by phosphorization.[6,8] Since large amounts of additional P sources, such as sodium or ammonium hypophosphite, are necessary in the phosphorization step with high P/M molar ratios up to 40:1[9,13,14] resulting in a significant waste of phosphorus resources and the release of flammable and poisonous phosphine gas, the method has significant environmental impacts. A more eco-friendly strategy has been developed for the direct production of TMP@C by annealing metal-organophosphine frameworks (MOPFs), which contain

[a] Dr. A. G. Mahmoud, Dr. M. J. Ferreira, Dr. M. F. C. Guedes da Silva, Dr. A. J. L. Pombeiro
Centro de Química Estrutural, Institute of Molecular Sciences, Instituto Superior Técnico, Universidade de Lisboa,Lisbon, Av. Rovisco Pais, 1049-001 Lisboa, Portugal.
E-mail: abdallah.mahmoud@tecnico.ulisboa.pt

[b] Dr. A. G. Mahmoud
Department of Chemistry, Faculty of Science, Helwan University, Ain Helwan, Cairo 11795, Egypt.

[c] Dr. J. V. Nardeli
Centro de Química Estrutural, Institute of Molecular Sciences, DEQ, Instituto Superior Técnico, Universidade de Lisboa, Av Rovisco Pais, 1049-001 Lisboa, Portugal.
E-mail: jeh.nardeli@gmail.com

[d] Dr. A. M. Ferraria, Dr. A. M. Botelho do Rego
BSIRG, IBB - Institute for Bioengineering and Biosciences, Instituto Superior Técnico, Universidade de Lisboa,Lisbon, 1049-001 Lisboa, Portugal.

[e] Dr. A. M. Ferraria, Dr. A. M. Botelho do Rego
Associate Laboratory i4HB–Institute for Health and Bioeconomy at Instituto Superior Técnico, Universidade de Lisboa, Av. Rovisco Pais, 1049-001 Lisboa, Portugal.

[f] Dr. A. M. Ferraria, Dr. A. M. Botelho do Rego, Dr. M. F. C. Guedes da Silva
Departamento de Engenharia Química, Instituto Superior Técnico, Universidade de Lisboa, Av. Rovisco Pais, 1049-001 Lisboa, Portugal.

Supporting information for this article is available on the WWW under https://doi.org/10.1002/batt.202300564

phosphine compounds as bridging organic linkers.[15–17] This approach eliminates the need for additional phosphorus sources and avoids the intensive release of phosphine gas during synthesis. One of the organophosphines that has recently been used is 1,3,5-triaza-7-phosphaadamantane (PTA, Figure 1), where carbon-confined copper phosphide (Cu_3P) nanosheets were prepared by annealing Cu–PTA MOPFs without the addition of other phosphorus sources.[15,16] Due to the presence of N atoms in the structure of PTA, its utilization as an organic linker to obtain TMP@C through MOPF-derived strategy can give P,N-codoped carbon matrices, which promotes the electrochemical activity of TMPs due to the ability of heteroatoms to modify electronic structures and electrolyte wettability of carbon matrices.[13,17,18]

The hydrosoluble aminophosphine PTA and its derivatives have garnered significant interest in the field of organometallic chemistry with potential applications in catalysis, medicinal inorganic chemistry and photoluminescence.[19,20] Although they are multifunctional ligands, with several potential coordination sites, such as P, N and O,[20–23] they tend to coordinate through the soft donor P atom. Therefore, their coordination to noble metals with soft acidic character, such as Ru, Re, Rh, Pt, Pd, Ag and Au, have been intensively studied,[19,20] while, their coordination to the abundant low-cost first row transition metals is limited to soft low oxidation state metal ions such as Cu-(I),[20,24–27] Mn(I),[28] Ni(0) and Cr(0).[29] Recently, we developed a novel strategy to address this challenge by obtaining PTA derivatives via N-alkylation, which contain hard donor coordination sites (e.g. carboxylate group).[30,31] This approach enables the coordination of PTA derivatives through the hard donor coordination sites to the first-row transition metal ions Mn(II), Co(II) and Ni(II),[30] as well as post transition metals such as Sn(IV).[31] Using this strategy, the soft P atom remains free and ready for further coordination to a soft metal centre, providing the possibility of obtaining heterometallic coordination compounds that contain both soft and hard transition metal atoms.

Binary-metal phosphides can potentially offer synergistic effects from various transition metal elements, resulting in improved electrochemical reactivity, higher electronic conductivity, and more extensive redox reactions when compared to single-metal phosphides.[32–35] Due to the multiple oxidation states of different metal centres, binary-metal phosphides may also have higher capacity.[36] Given that the reported examples of TMP@C derived from MOPFs based on PTA are limited to Cu_3P as a single TMP,[15,16] the primary objective of this study is to explore the impact of incorporating a second metal into the Cu-PTA MOPFs on the electrochemical properties of the resulting NPs, to assess potential synergistic effects. In this context, this study describes a groundbreaking approach to

obtain novel heterometallic-organophosphine frameworks (HMOPFs) based on a PTA-core ligand using solvent-free, solid-state mechanochemical method through ball milling. The organophosphine linker, (PTA-CH_2-C_6H_4-*p*-COOH)Br (Figure 2), was chosen because it possesses both soft donor (P atom on the PTA cage) and hard donor (O atoms on the carboxylic acid group) sites, enabling selective coordination to the metal centres. Only abundant and low-cost first row transition metals have been employed, with Cu(I) to serve as the soft metal centre and Cu(II), Ni(II) and Zn(II) as the hard metal centres. The HMOPFs were pyrolyzed under N_2 atmosphere to obtain the bimetallic TMPs@C nanocomposites. Due to the presence of multiple heteroatoms in the organic linker used in this study, the resulting carbon matrices are multi-codoped with phosphorus, nitrogen, and bromine. Unlike conventional methods that require additional phosphorus sources or bromine vapours to prepare P- or halogen-doped carbon,[37,38] this approach does not rely on any external sources of these elements. The electrochemical performance was assessed by cyclic voltammetry (CV), galvanostatic charge-discharge (GCD) and cycling stability tests. The combination of all these techniques revealed insights on the electrochemical properties of the activated carbons materials for energy storage applications.

Results and Discussion

Synthesis of the HMOPFs [CuMBr$_2$(μ-1κP,2κOO'-PTA-CH$_2$-C$_6$H$_4$-*p*-COO)$_2$]$_n$·nBr (M≡Zn{II}, Ni{II} or Cu{II})

Recently, we described the reaction of [PTA-CH_2-C_6H_4-*p*-COOH]-Br with copper (I) bromide using 1:2 metal-to-ligand ratio to obtain [CuBr$_2$(μ-κ*P*-PTA-CH$_2$-C$_6$H$_4$-*p*-COOH)$_2$]Br (**1**), a complex in which the ligand coordinates to the soft Cu(I) centre through the P atom (Scheme 1, route 1).[39] Reacting zinc (II) acetate with two molar equivalents of [PTA-CH$_2$-C$_6$H$_4$-*p*-COOH]Br in methanol at room temperature resulted in the formation of [Zn(μ-κ*OO'*-PTA-CH$_2$-C$_6$H$_4$-*p*-COO)$_2$]Br$_2$ (**2**), where the ligand coordinates to the hard Zn(II) centre through the O atoms of the carboxylate group (Scheme 1, route 2). In complex **2**, the P coordination sites remain unoccupied, which offers the potential for binding to a soft metal centre and the formation of heterometallic (hard/soft metal centres) coordination compounds. The reactions depicted in Scheme 1 demonstrate the ability of the aminophosphine PTA ligand functionalized with a hard donor
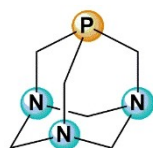

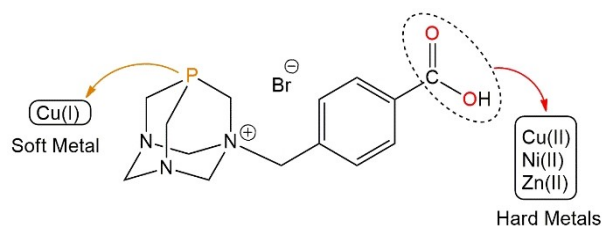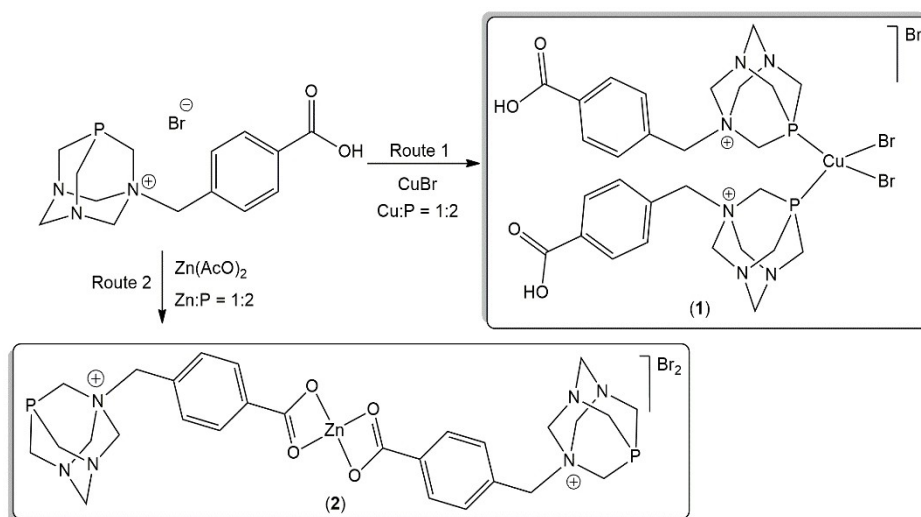**Figure 1.** 1,3,5-triaza-7-phosphaadamantane (PTA).

Figure 2. The organophosphine linker, (PTA-CH$_2$-C$_6$H$_4$-*p*-COOH)Br, used in this study.
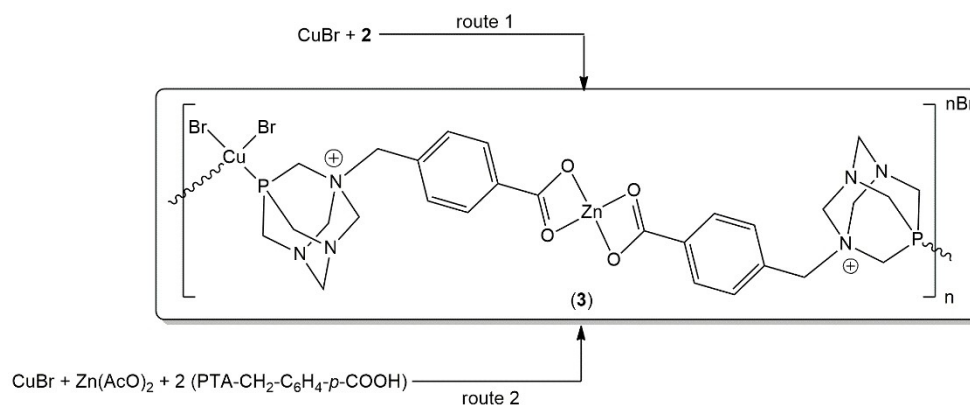
Scheme 1. Synthesis of the Cu(I) complex **1** and Zn(II) complex **2**.

moiety to adapt its coordination behaviour according to the type of metal involved. The proposed formulation of the water-soluble compound **2** was confirmed using elemental analysis, FTIR, NMR spectroscopy (^{1}H, ^{13}C{^{1}H} and ^{31}P{^{1}H}; Figures S1–S6) and ESI-MS.

To enhance the sustainability of HMOPFs production, a solvent-free approach was employed to obtain the bimetallic Cu(I)/Zn(II) MOPF through mechanochemical synthesis. Reacting equimolar amounts of CuBr and **2** in a planetary ball mill resulted in the formation of [CuZnBr$_2$(μ-1κP,2κOO'-PTA-CH$_2$-C$_6$H$_4$-p-COO)$_2$]$_n$·nBr (**3**) coordination polymer (Scheme 2, route 1) in 75% yield after 4 h. The coordination of the P atom in **2** to the Cu(I) centre was confirmed using solid-state NMR. The ^{31}P NMR spectrum of **3** shows a peak at −76.78 ppm, downfield shifted from that of compound **2** (−89.13 ppm) due to the coordination of the P atom to the Cu(I) metal centre (Figure S7). The molecular formula of **3** was confirmed by elemental analysis and ICP measurements of the Cu and Zn metals that showed a 1:1 molar ratio. In order to eliminate the preparation step of compound **2** in methanol, and obtain the HMOPF in a

one-pot, three-component reaction using solvent-free conditions, the metal salt precursors CuBr and Zn(AcO)$_2$ were mixed with the ligand (PTA-CH$_2$-C$_6$H$_4$-p-COOH)Br using the molar ratio Cu:Zn:P of 1:1:2 in the ball mill to obtain **3** in 64% yield after 4 h (Scheme 2, route 2).

Using the same synthetic procedure, HMOPFs combining soft/hard metal centres of Cu(I)/Ni(II) and Cu(I)/Cu(II) were prepared via three-component mechanical ball milling of the pro-ligand (PTA-CH$_2$-C$_6$H$_4$-p-COOH)Br with the metal salt precursors CuBr and Ni(AcO)$_2$ or Cu(AcO)$_2$ to obtain [CuMBr$_2$(μ-1κP,2κOO'-PTA-CH$_2$-C$_6$H$_4$-p-COO)$_2$]$_n$·nBr (M=Ni^{2+} for **4** or Cu^{2+} for **5**; Figure 3). The proposed chemical formula were confirmed by elemental analysis and ICP experiments. The P–Cu(I) coordination bond in **4** was confirmed by solid-state ^{31}P NMR, which showed a quartet peak centred at δ −80.4 (Figure S8) as a consequence of spin-spin coupling between ^{31}P ($I = 1/2$) and ^{63}Cu/^{65}Cu ($I = 3/2$).[40–42] The quadrupolar copper centre distorts the quartet and thus linespacing is uneven; −73.0, −77.9, −83.2 and −88.2 ppm, with $\Delta_{21}=994$ Hz, $\Delta_{32}=1067$ Hz and $\Delta_{43}=1021$ Hz, giving an average linespacing $<\Delta\nu> = 1028$\Hz and

Scheme 2. Synthesis of the bimetallic Cu(I)/Zn(II) coordination polymer (**3**) in solvent-free conditions via mechanical ball milling.
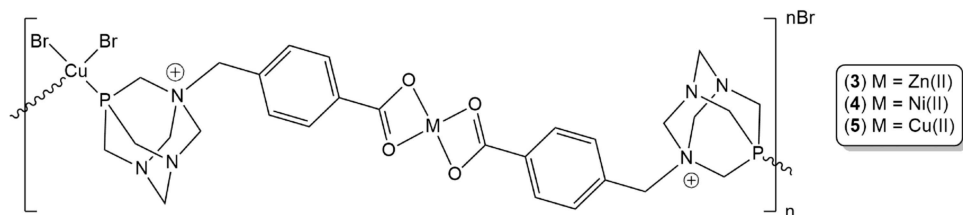
Batteries & Supercaps

Research Article
doi.org/10.1002/batt.202300564

**Chemistry
Europe**
European Chemical
Societies Publishing

Figure 3. Schematic illustration of HMOPFs **3**–**5**.

an asymmetry parameter, defined by the difference between the maximum and minimum Δv values, of 73 Hz.[40] This is a consequence of a non-symmetrical coordination sphere that gives rise to a non-zero quadrupolar constant. The $^1J_{Cu-P}$ is 1037 Hz (estimated by $J=(\Delta_{21}+2\ \Delta_{32}+\Delta_{43})/4$).[41] This value is smaller than those found in reported Cu(I) complexes supported either by aromatic phosphines,[40] aliphatic phosphines,[41] or other ligands.[42] The same trend is observed in the dv_{Cu} parameter, obtained by multiplying d ($d=(\Delta_{43}-\Delta_{21})/4$) by the Zeeman frequency of ^{63}Cu, that is used by Bowmaker *et al.* to compare spectra obtained at different field strengths.[41] We obtain for dv_{Cu} of **4** the value of 7.39×10^9 Hz, one order of magnitude smaller than for complexes with two phosphines.[41] We tentatively explain this by the presence of a positive charge on the ligand that hampers the donation ability of the phosphorus of the PTA fragment.

The microstructures and morphologies of the synthesised HMOPFs **3**–**5** were investigated by scanning electron micro-scopy (SEM) equipped with energy dispersive X-ray spectro-scopy (EDS). The SEM images of HMOPFs (Figure 4, images a, d and g) show block morphologies with irregular appearance of different sizes. EDS (Figure 4; Tables S1–S3 and Figures S9–S14) shows the uniform distribution of the metal centres and confirms the presence of the organophosphine linker components C, N, Br, O and P at the surface of the particles.

Synthesis of Cu–M@C materials

The transition metal NPs embedded in multi-P,N,Br-codoped carbon matrices were obtained by annealing HMOPFs **3**–**5** at 800 °C, under the continuous flow of N_2 gas, to afford the Cu–Zn@C, Cu–Ni@C and Cu–Cu@C composites, respectively. Thermal gravimetric analysis (TGA) of the HMOPFs under N_2 flow was used to determine the pyrolysis process, where a region of significant weight loss was identified around 750 °C.
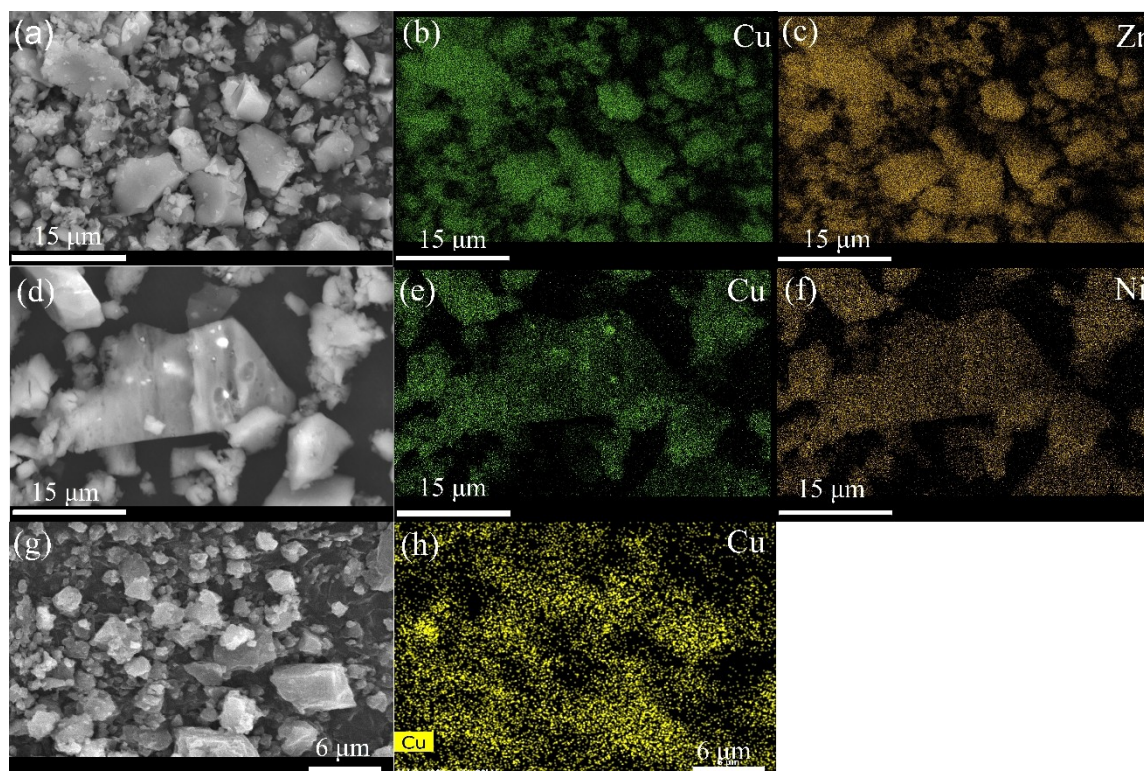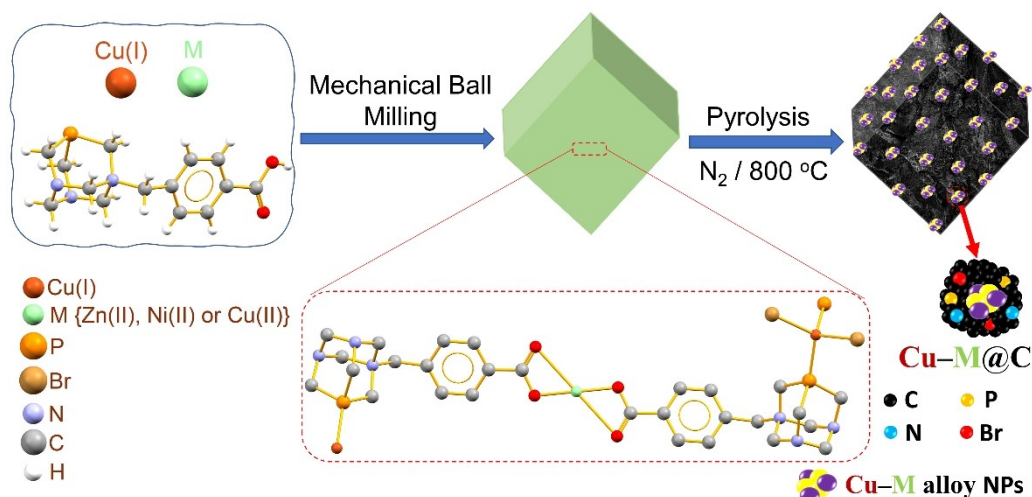

Figure 4. SEM images (a, d and g) and the corresponding elemental mapping of metal centres using EDS (b, c, e, f and h) of HMOPFs **3** (a–c), **4** (d–f) and **5** (g–h).

Batteries & Supercaps

Research Article
doi.org/10.1002/batt.202300564

Chemistry Europe
European Chemical
Societies Publishing

Scheme 3. Schematic illustration for the formation of Cu–M@C nanocomposites.

Scheme 3 shows the Cu–M@C composites prepared using a facile HMOPF-derived approach, which involves the mechano-chemical synthesis of Cu(I)–M HMOPFs and the subsequent pyrolysis process.

The X-ray diffraction (XRD) patterns of the Cu–M@C composites revealed the presence of multi-M/P phases obtained from the pyrolysis of HMOPFs (Figure 5 and Figures S21–S23). The XRD patterns of the HMOPFs against their pyrolyzed corresponding composites are depicted in Figure S24 to display the transformation process. The XRD pattern of Cu–Zn@C exhibited diffraction peaks matching well with copper phosphide (Cu_3P, COD 1527899)[43] and zinc pyrophosphate (α-$Zn_2P_2O_7$, COD 1528830)[44] phases. The XRD pattern of Cu–Ni@C showed a set of peaks that corresponded to metal phosphides, namely Cu_3P (COD 1527899)[43] and Ni_2P (COD 1522619),[45] in addition to the cupric pyrophosphate ($Cu_2P_2O_7$, COD 9007764)[46] phase. The XRD pattern of Cu–Cu@C depicted diffraction peaks matched also copper phosphide (Cu_3P, COD 1527899)[43] phase, as well as cupric phosphate ($Cu_3O_8P_2$, COD 1200002)[47] and pyrophosphate (β-$Cu_2P_2O_7$, COD 1538528)[48]

Figure 5. XRD patterns of Cu–Zn@C (left), Cu–Ni@C (middle) and Cu–Cu@C (right).

Batteries & Supercaps

Research Article
doi.org/10.1002/batt.202300564

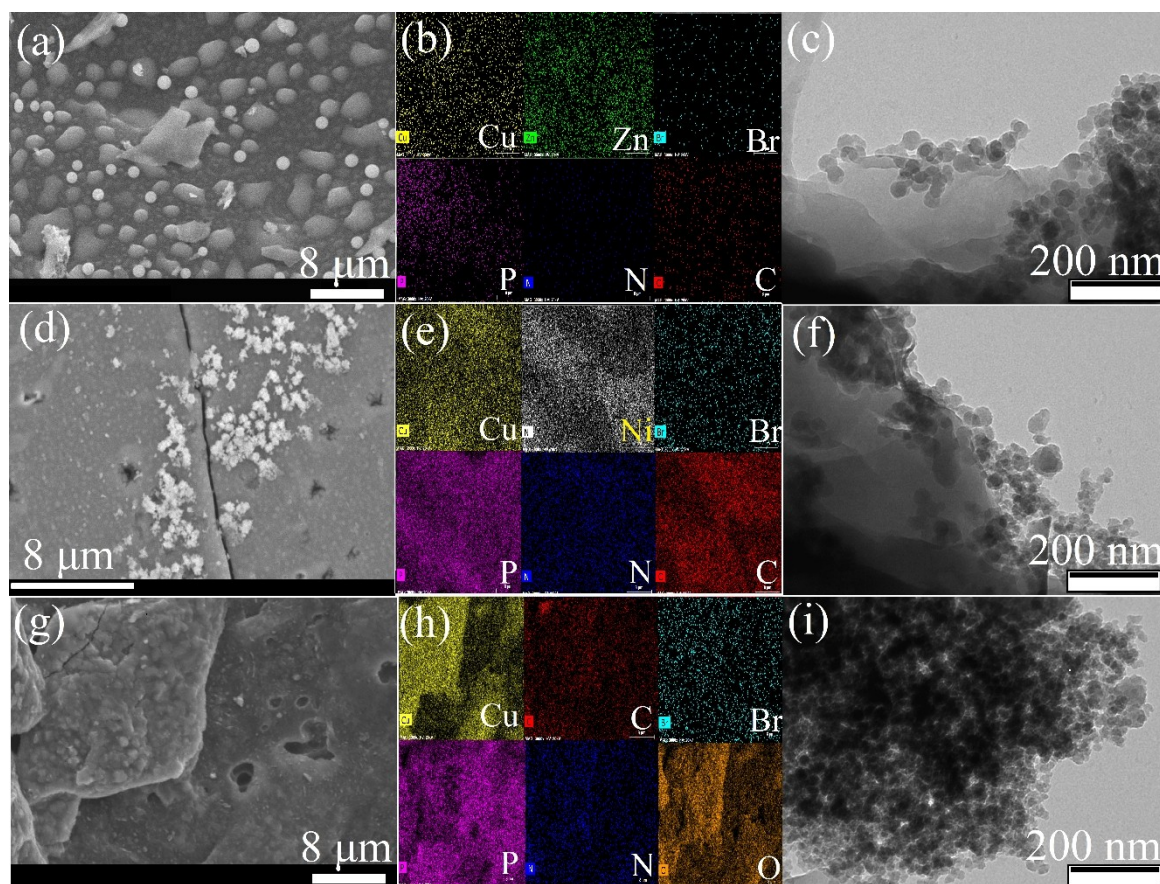**Chemistry Europe**
European Chemical
Societies Publishing

Figure 6. SEM images (a, d and g) with the corresponding elemental mapping using EDS (b, e and h) and TEM images (c, f and i) of Cu–Zn@C (a-c), Cu–Ni@C (d-f) and Cu–Cu@C (g–i).

phases. The pyrolysis of the HMOPFs was performed in inert atmosphere to obtain the TMPs and avoid the formation of metal oxides. However, the formation of phosphate phases seems to be inevitable due to the presence of the O-atoms of the carboxylate group at the HMOPF precursors.

The surface morphology of the carbon embedded NPs was investigated by SEM equipped with EDS, and TEM. The obtained composites maintained similar particle shapes of the corresponding original HMOPFs, but with their lengths and thickness decreased due to the volume shrinkage during pyrolysis. Additionally, NPs were observed on the surface of the composites. The SEM image of Cu–Zn@C (Figures 6a) exhibited the formation of spherical particles agglomerated on the surface with also some looming particles embedded in the carbon matrix. The Cu–Ni@C composite had a sparsely decorated surface with sesame-like particles (Figure 6d). The Cu–Cu@C composite showed embedded looming particles within the carbon matrix (Figure 6g). The elemental mapping images (Figures 6b, 6e and 6 h) usings EDS pointed out a highly uniform distribution of the Cu–M alloy NPs in the multi-P, N, Br-codoped carbon matrices. The atomic and weight concentrations on the surface of the composites showed significant changes in the contents of organic ingredients (Tables S1–S6 and Figures S9–S20), which confirm the decomposition of the HMOPF precursors into the Cu–M NPs and carbon matrices. The

TEM images (Figures 6c, 6f and 6i) of the carbon confined Cu–M NPs show spherical, slightly irregular, shaped granules with diameters lower than 50 nm in the carbon matrices.

The surface properties of the HMOPFs and Cu–M@C materials were assessed by N_2 adsorption measurements at $-196\,°C$, after degassing the samples at $120\,°C$ under dynamic vacuum. The results presented in Table 1 revealed the development of the textural characteristics (BET surface are and total pore volume) with the pyrolysis process. While the HMOPFs are non-porous with BET surface areas around $7\,m^2g^{-1}$, the Cu–M@C exhibited a significant increase in BET surface area

Table 1. BET surface area and porosity of HMOPFs and Cu–M@C nanocomposites by adsorption of N_2 at $-196\,°C$: surface area (S_{BET}), total pore volume (V_p), micropore volume (V_{mic}), average pore diameter (d).

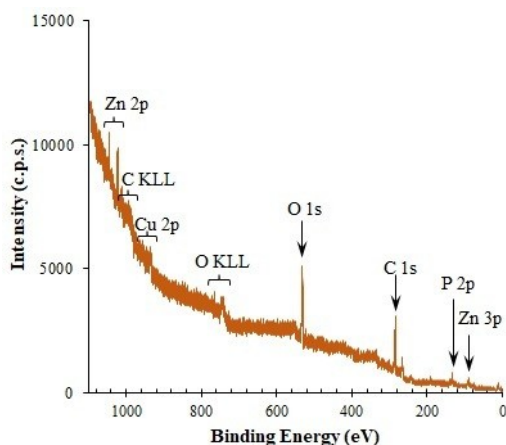| HMOPF	S_{BET} m^2g^{-1}	V_p cm^3g^{-1}	V_{mic} cm^3g^{-1}	d Å
3	7.5	0.017	0.001	184.5
4	6.4	0.010	0.002	85.6
5	6.6	0.017	0.001	130.0
Cu–Zn@C	415	0.181	0.127	29.8
Cu–Ni@C	284	0.163	0.102	30.3
Cu–Cu@C	280	0.155	0.100	29.4

Figure 7. XPS spectrum of Cu–Zn@C.

ranging from 280 to 415 $m^2 g^{-1}$, along with a total pore volume of 0.15–0.18 $cm^3 g^{-1}$. The shape of the adsorption-desorption isotherms (Figure S25) indicated the microporous nature of the Cu–M@C materials, which exhibit type I isotherm with H4 hysteresis associated with narrow slit pores, according to IUPAC classifications.

The Cu–M@C composites were also analysed by XPS. The results for the composite with higher performance are here described. The complete set of XPS results is included in Supplementary Information. The detected elements for Cu–Zn@C composite were Cu, Zn, P, N, C, and O (Figure 7). The studied XPS regions Cu 2p, Zn 2p, N 1s, C 1s and O 1s are presented in Figure 8 and Tables 2 and S7. C 1s was fitted with five peaks. The peak at the lowest binding energy was set to 284.4 eV (graphitic carbon)[49] and used as reference for the binding energy shift due to the accumulation of charge resulting from the electron ejection. The peak at 285.4 eV is partly due to the vibrational losses typical of graphite and partly to C bonded to N. At 286.7 eV and 288.2 eV, peaks assignable, respectively, to carbon singly bonded to oxygen and to carbonyl and/or ester groups were also fitted. Finally, the energy loss associated to a $\pi \rightarrow \pi^*$ transition is centred at 290.4 eV. For oxygen, O 1s was fit with four components centred at 530.3, 531.6, 532.9 and 534.5 eV assignable, respectively, to O^{2-} in metallic oxides, O bonded to P, a mixture of O singly and doubly bonded to carbon, and water. P 2p was fit to two doublets having a spin-orbit split of 0.87 eV. The main one has the most intense component, P $2p_{3/2}$, centred at 133.6 eV, typical of phosphate (PO_4^{3-}) or diphosphate ($P_2O_7^{4-}$) ions. A tiny doublet with P $2p_{3/2}$ centred at 131.5 eV is assignable to P bonded to C.[50] N 1s photoelectron region was fit with four peaks centred at 398.1 eV, 399.1 eV, 400.8 eV, and 406.0 eV assignable, respectively, to pyridinic, amine, graphitic,[49] and nitrate ion, NO_3^-.[50] Zn $2p_{3/2}$ is centred at 1022.5 eV, assignable to Zn^{2+}. Finally, Cu $2p_{3/2}$ was fitted with a set of peaks corresponding to the main peak and the multiplet structure typical of the Cu in the oxidation state 2+. Bromine is detected in residual amounts (Table S7 and Figure S26), which means that it is almost absent at the extreme surface (*i.e.* within
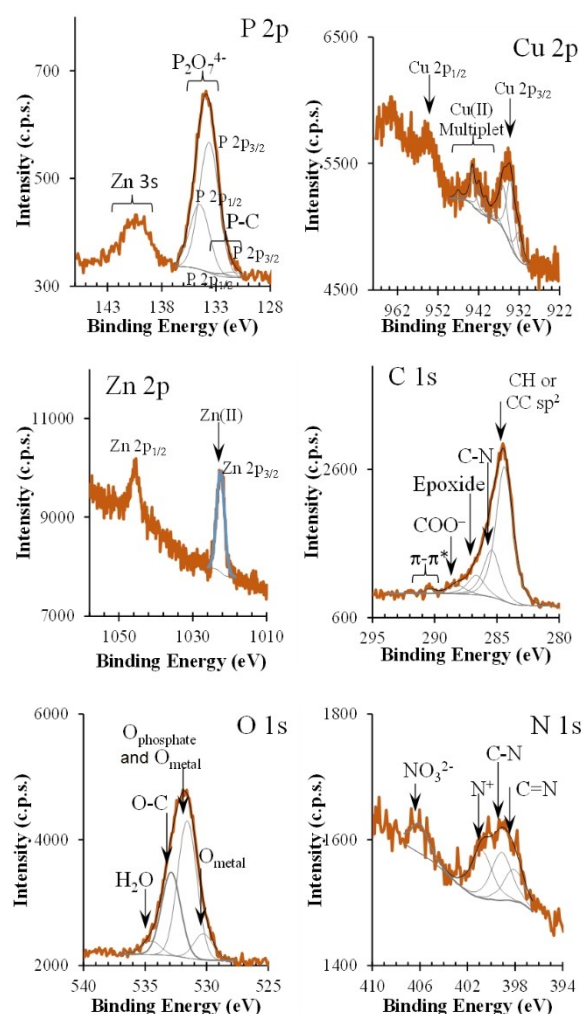

Figure 8. XPS regions of Cu–Zn@C: P 2p, Cu 2p, Zn 2p, C 1s, O 1s and N 1s.

the XPS probing layer which is shallower than the one probed by EDS).

The quantitative study confirms the presence of zinc pyrophosphate ($Zn_2P_2O_7$) at the powder surface (as observed in

Table 2. XPS atomic concentrations (%) and relevant atomic ratios.

Element	Cu–Zn@C
C	49.9
O	32.8
N	3.4
P	4.9
Zn	5.1
Cu	3.9
Atomic ratios	
Zn/P	1.1
$(O_{metal\ and\ phosphates})/(Cu + P_{phosphate} \times 3.5)$	1.0
$O_{phosphates}/P_{phosphates}$	3.7

Batteries & Supercaps

Research Article
doi.org/10.1002/batt.202300564

Chemistry Europe
European Chemical
Societies Publishing

bulk by XRD), but not copper phosphide (Cu_3P). In Table 2, the computed atomic ratios attest the surface composition: Zn/P = 1.09; ($O_{metal\ and\ phosphate}$)/(Cu + $P_{phosphate}$×3.5) = 1.0, where $O_{metal\ and\ phosphate}$ and $P_{phosphate}$ are identified in Table S7 and Figure 8; and $O_{phosphate}/P_{phosphate}$ = 3.7 are compatible with the presence of $Zn_2P_2O_7$ and CuO. No phosphorus with a $2p_{3/2}$ component at a binding energy typical of phosphides (128–130 eV)[50] is detected. Therefore, at the extreme surface of the powder there is no Cu_3P, contrarily to the result obtained in volume by XRD. Actually, copper is mainly in the form of Cu(II) oxide, as shown by the Cu 2p region which includes a multiplet structure, centred at the higher binding energy side of the Cu $2p_{3/2}$ photoelectron peak (Figure 8), typical of transition metal atoms with unpaired electrons in the valence band.[51] Its absence in XRD pattern means that this oxide is mainly at the surface of the powder. The ratio Zn/P = 1.09 shows that zinc is in a slight

excess, possibly bonded to nitrate groups, which are detected in N 1s (Figure 8).

Electrochemical study

The electrochemical performance of the Cu–M@C composites was assessed as an active electrode material for pseudocapacitor applications. Figure 9 illustrates the electrochemical results obtained for the different electrode materials, with Figures 9a and 8b showcasing the cyclic voltammetry (CV) curves at a scan rate of 50 mV s^{-1}, and the galvanostatic charge-discharge (GCD) curves obtained at 2 A g^{-1}, respectively. From Figure 9a, it is evident that the CV curves for all the materials display redox behaviour that are however more evidenced in the presence of Ni. In Figure 9b, the potential window for the Cu–Zn@C electrode is approximately 1.25 V, which is superior to the other
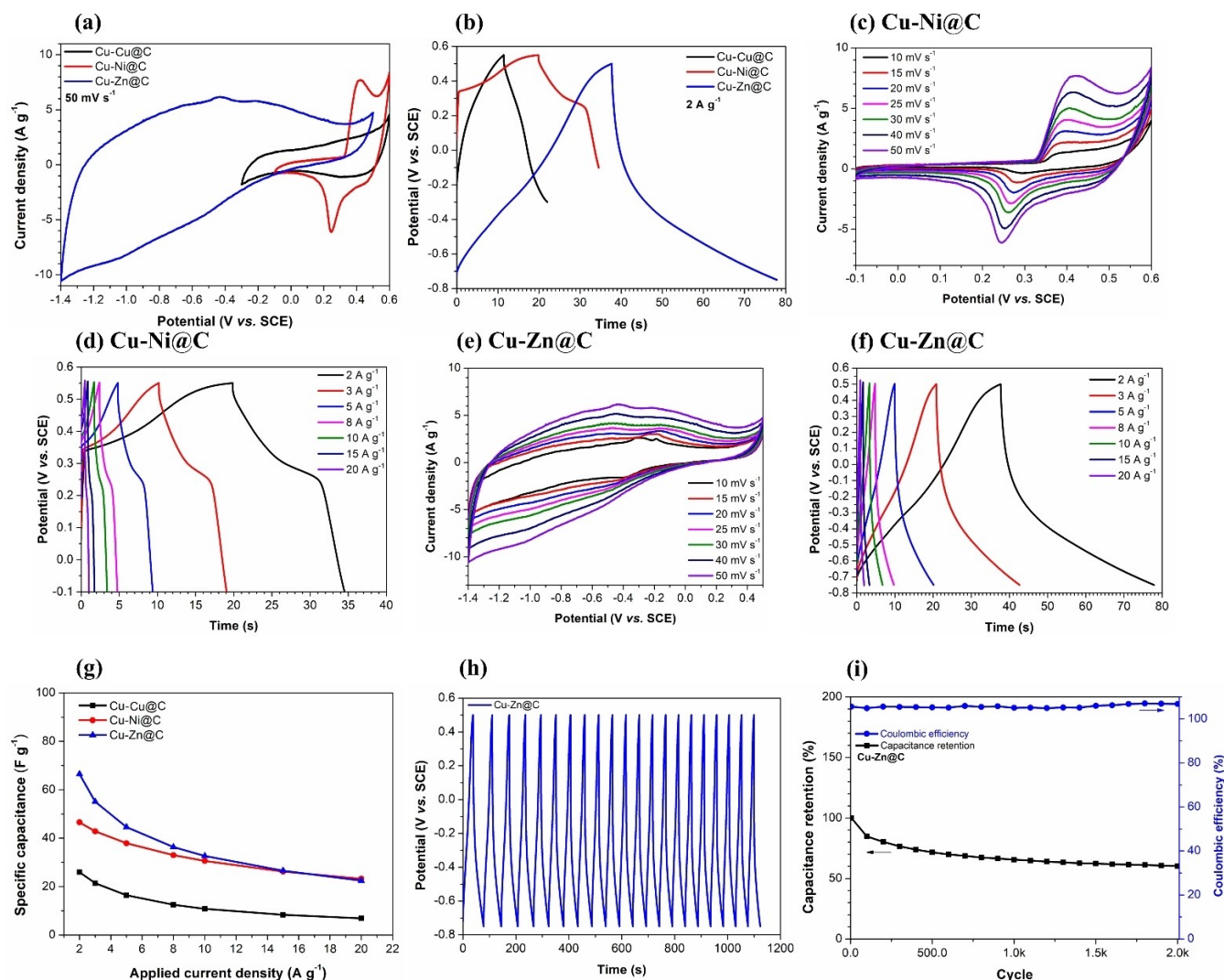

Figure 9. Comparison CV (a) and GCD (b) curves of Cu–Cu@C, Cu–Ni@C, Cu–Zn@C electrodes at 50 mV s^{-1} and 2 A g^{-1}. (c) CV and (d) GCD curves of the Cu–Ni@C electrode at different scan rates and different current densities. (e) CV and (f) GCD curves of the Cu–Zn@C electrode at different scan rates and different current densities. (g) Specific capacitance contrast diagram of Cu–Cu@C, Cu–Ni@C, and Cu–Zn@C electrodes at different current densities. (h) Cyclic stability (2k cycles at 2 A g^{-1}) of the Cu–Zn@C electrode. (i) Comparison of the variation of capacitance retention and coulombic efficiency as a function of cyclic numbers, 2k cycles in a 2 M KOH electrolyte.

Batteries & Supercaps

Research Article
doi.org/10.1002/batt.202300564

**Chemistry
Europe**

European Chemical
Societies Publishing

electrodes (Cu–Ni@C with potential window 0.7 V and Cu–Cu@C with potential window 0.9 V, Supplementary material). The Cu–Zn@C electrode is therefore active in a larger potential window and the results indicate that this composite can serve as electroactive material for negative electrodes in asymmetric pseudocapacitors.

Figures 9c and 9d depict the CV and GCD curves of the Cu–Ni@C electrode at different scan rates (10, 15, 20, 25, 30, 40, and 50 mV s^{-1}) and at different current densities (2, 3, 5, 8, 10, 15, and 20 A g^{-1}), respectively. As seen in Figure 9c, with the increase in scan rate the position of the anodic peak shifts to higher potential and that of the cathodic peak to lower potential. The redox peak and nonlinear charge–discharge curve in Figure 9d indicate the faradaic nature of the electrode, which is also evidenced in the GCD where a plateau can be observed, as expected for a material of faradic and "battery like" nature. As the scan rate increased there is the onset of a resistive feature close to the anodic limits.

Figure 9e displays the CV curves of the Cu–Zn@C electrode at different scan rates (10, 15, 20, 25, 30, 40, and 50 mV s^{-1}). Figure 9f exhibits the GCD curves of the Cu–Zn@C electrode at different current densities (2, 3, 5, 8, 10, 15, and 20 A g^{-1}).

It can be observed that, with the increase in scan rate, all CV curves of the Cu–Zn@C electrode maintain almost the same shape. The GCD curves retain their general shape with the change of current density.

Figure 9g presents a comparison of the specific capacitance of the three electrodes under different current densities. The specific capacitance of the Cu–Zn@C electrode is 66.5 F g^{-1} at the current density of 2 A g^{-1}, whereas the Cu–Ni@C electrode achieves 46.5 F g^{-1} and the Cu–Cu@C electrode 26 F g^{-1}.

Figure 9h displays the cycling stability tests performed using continuous GCD at 2 A g^{-1} for 2 k cycles for the Cu–Zn@C electrode in 2 M KOH. The response (Figure 9i) demonstrates a good cycling stability, with a capacitance retention rate of approximately 60% and high coulombic efficiency. The high (above 100%) coulombic efficiency values and their constancy with the number of cycles deserve some considerations. Since the starting and final voltage limits were strictly controlled (see Figure 9h), we rule out any difference in the charge and discharge method which could result in the overestimation of that parameter. However, one cannot exclude the occurrence of a side reaction in the discharge period that, without affecting the potential, would consume current. Further discussion would be on this subject will be, at this stage, too speculative. The high coulombic efficiency may also be associated with the increased wettability that leads to a better electrode-electrolyte interaction with time. The larger working potential window, together with the good capacitance and stable coulombic efficiency are comparable with other negative/positive TMP-based electrodes for asymmetric supercapacitors (like Cu$_3$P, CoP, FeP, FeCoCuP),[52–56] which makes this material an interesting candidate as negative electrode for asymmetric supercapacitor assemblies.

Highly porous structures with a substantial surface area can optimize the exposure of active sites to the electrolyte. Therefore, in addition to the distinctive structural features, the high

electrochemical efficiency of Cu–Zn@C, in comparison to Cu–Ni@C and Cu–Cu@C counterparts, can also be attributed to its higher surface area (Table 1). XPS results show that Cu–Zn@C has the lowest Metal/C atomic ratio and the highest O/Metal ratio compatible with a higher content in metal hydroxides.

Experimental

All reagents and solvents were obtained from commercial sources and used as received without further purification. [PTA-CH$_2$-C$_6$H$_4$-p-COOH]Br was obtained according to the reported procedure.[57] IR spectra (4000–400 cm^{-1}) were obtained on Cary 630 FTIR Spectrometer (Agilent Technologies, Santa Clara, CA, USA). Electrospray mass spectra were obtained with a Varian 500-MS LC Ion Trap Mass Spectrometer (Agilent Technologies, Santa Clara, CA, USA) equipped with an electrospray ion source. The Inductively Coupled Plasma (ICP) and C, N, and H elemental analyses were performed by the Microanalytical Service (at Laboratório de Análises) of Instituto Superior Técnico (IST).

The surface morphology of the materials was determined by a scanning electron microscope (SEM) Hitachi S2400 (Tokyo, Japan) with Bruker light elements energy dispersive X-ray spectroscopy (EDS) detector and a transition electron microscope (TEM) Hitachi 8100 (Tokyo, Japan) with ThermoNoran light elements at IST MicroLab.

Multi-nuclear NMR spectra (^{1}H, ^{13}C, ^{31}P) were obtained from a 300 MHz spectrometer (Bruker Avance II, Bruker, Billerica, MA, USA) at ambient temperature. Chemical shifts δ are quoted in ppm, and coupling constants given in Hz. The ^{1}H and ^{13}C NMR spectra were internally referenced to residual protio-solvent resonance and are reported relative to tetramethylsilane ($\delta=0$); ^{31}P chemical shifts were referenced with external 85% H$_3$PO$_4$. Assignments of some ^{1}H and ^{13}C signals rely on g-COSY and g-HSQC experiments.

Solid state NMR spectra were recorded in a Bruker AVANCE III 500 spectrometer, operating at B$_0$ field of 11.7 T, with ^{1}H, ^{13}C and ^{31}P Larmor frequencies of 500.1, 125.8 and 202.5 MHz, respectively. All experiments were performed in a 4 mm double-resonance MAS probe (Bruker) at 296 K. Samples were packed into ZrO$_2$ rotor with Kel-F caps and spinned at 5 KHz. Spectra were referenced externally to TMS (for ^{1}H, 0 ppm) and glicine (for ^{13}C, C=O at 176.03 ppm) and ADP (ammonium dihydrogen phosphate NH$_4$H$_2$PO$_4$) for ^{31}P (0 ppm). The ^{13}C CPMAS spectra were acquired using the TOSS sequence to suppress spinning side-bands,[58] using phase cycling as described in the literature.[59] For ^{13}C CPMAS the following conditions were used: the ^{1}H 90° pulse was set to 2.5 µs corresponding to a rf of ~100 kHz. The CP step was performed with a contact time (CT) of 2000 µs using a 50–100% RAMP shape at the ^{1}H channel and using a 50 kHz square shape pulse on the ^{13}C channel; RD was 5 s. During the acquisition, a SPINAL-64 decoupling scheme was employed using a pulse length for the basic decoupling units of 5 µs at rf field strength of 100 kHz. The ^{31}P CPMAS spectra were obtained using the following conditions: the ^{1}H 90° pulse was set to 2.5 µs corresponding to a rf of ~100 kHz. The CP step was performed with a contact time (CT) of 5000 µs using a 50–100% RAMP shape at the ^{1}H channel and using a 100 kHz square shape pulse on the ^{31}P channel; RD was 5 s. During the acquisition, a SPINAL-64 decoupling scheme was employed using a pulse length for the basic decoupling units of 2.5 µs.

TGA tests were performed under N$_2$ flow using a STA 6000 simultaneous thermal analyzer from PerkinElmer.

N_2 adsorption measurements were performed at $-196\,°C$ using Micrometrics ASAP 2060 gas sorption instrument (Hiden Isochema, Warrington, UK).

Powder XRD patterns were collected using a Bruker D8 ADVANCE Powder Diffractometer, with Cu radiation in a Bragg Brentano geometry.

XPS analyses were conducted with a non-monochromatic dual anode KRATOS spectrometer (Manchester, UK), model XSAM 800. Conditions of spectral acquisition, equipment operation and data treatment were as previously reported.[31] Binding energies were corrected from the charge shift using as reference the binding energy (BE) = 284.4 eV, found for sp^2 carbon atoms in extended delocalized systems.[49]

For the mechanochemical reactions, the planetary high energy ball mill Emax (Retsch Haan, Germany) was used. The mill has two stainless steel milling jars (125 mL) rotating around its axis which are partially filled with stainless steel milling balls (3 mm diameter).

The pyrolysis of HMOPFs was performed in a tube furnace (TF 12/60/300, Carbolite Gero, United Kingdom) that featured a working tube with end seals and gas inlet/outlet pipe for N_2 gas flow.

Synthesis of [Zn(L^1)$_2$]Br$_2$ (2)

To a methanol solution (30 mL) of [PTA-CH$_2$-C$_6$H$_4$-p-COOH]Br (0.6 mmol, 220 mg, 2 equiv.) was added $Zn(CH_3COO)_2.2H_2O$ (0.3 mmol, 66 mg, 1 equiv.) in methanol (20 mL) dropwise with stirring. The produced white precipitate compound 2 was stirred at room temperature overnight, and then filtered off, repeatedly washed with acetone and dried under vacuum.

Yield = 49.5% (120 mg) based on the metal salt. Elemental analysis calcd (%) for $C_{28}H_{36}Br_2N_6O_4P_2Zn$: C 41.63, H 4.49, N 10.40; found: C 41.51, H 4.43, N 10.34. FTIR (KBr): ν (cm^{-1}) = 3854 br m, 2791 br s, 1600 s, 1558 s, 1457 w, 1407 s, 1313 m, 1215 w, 1190 w, 1123 m, 1075 m, 1033 m, 978 w, 928 w, 903 w, 884 w, 852 m, 814 m, 801 w, 783 m, 765 m, 734 m, 694 w, 560 w, 456 w. ^{1}H NMR (300 MHz, DMSO-d_6, δ)/COSY: 8.02 (d, J = 7.8 Hz, 2H, Ar–H, CH–C–COOH), 7.53 (d, J = 8.1 Hz, 2H, Ar–H, CH–C–CH$_2$), 5.06 (d, J = 11.4 Hz, 2H, NCH_2N$^+$), 4.86 (d, J = 11.1 Hz, 2H, NCH_2N$^+$), 4.54 (d, J = 13.2 Hz, 1H, NCH_2N), 4.36 (d, J = 13.2 Hz, 1H, NCH_2N), 4.23 (d, J = 5.7 Hz, 2H, PCH_2N$^+$), 4.15 (s, 2H, CCH_2N$^+$), 3.93–3.75 (m, 4H, PCH_2N). ^{31}P{^{1}H} NMR (300 MHz, DMSO-d_6, δ): −83.61. ^{13}C{^{1}H} NMR (300 MHz, DMSO-d_6, δ)/DEPT/HSQC: 169.84 (COO$^-$), 137.46 (C_{quat}–CH$_2$), 132.56 (CH–C–CH$_2$), 129.90 (CH–C–COO$^-$), 127.97 (C_{quat}-COO$^-$), 78.82 (NCH$_2$N$^+$), 69.34 (NCH$_2$N), 64.49 (CCH$_2$N$^+$), 51.75 ($^1J_{pc}$ = 128.1, PCH$_2$N$^+$), 45.41 ($^1J_{pc}$ = 81, PCH$_2$N). DEPT (300 MHz, DMSO-d_6, δ): 132.34, 129.66, 78.58, 69.11, 64.23, 51.50, 45.16. ^{31}P ssNMR (202.5 MHz, δ): −89.13. ^{13}C ssNMR (125.8 MHz): 170.66 (COO), 141.31 (C–Ar), 135.37 (C–Ar), 134.44 (C–Ar), 131.43(C–Ar), 130.40 (C–Ar), 130.09 (C–Ar), 81.20 (NCH$_2$N$^+$), 79.78 (NCH$_2$N$^+$), 73.83 (NCH$_2$N), 67.41 (CCH$_2$N$^+$), 51.28 (PCH$_2$N$^+$), 50.64 (PCH$_2$N$^+$), 48.65 (PCH$_2$N). ESI(+)-MS in H_2O (m/z assignment, % intensity): 953 ([M+Zn+Br]$^+$, <5), 806 (M$^+$, <5), 727 ([Zn(L^1)$_2$Br]$^+$, <5), 436 ([Zn(L^1) Br]$^+$, 7), 292 ([HL^1]$^+$, 100).

Synthesis of HMOPFs

Synthesis of ([CuBr$_2${PTA-CH$_2$-C$_6$H$_4$-p-COO}$_2$Zn]Br)$_n$ (3)

Method 1. To a 125 mL stainless steel grinding jar (RETSCH), compound 2 (500 mg, 0.62 mmol, 1 equiv.) and CuBr (88.9 mg, 0.62 mmol, 1 equiv.) were added, together with 20 stainless steel balls (3 mm diameter). The mixture was milled at 650 rpm for 4 hours. The resulting product was retrieved from the jar and balls

by dispersing it into a minimum volume of methanol. The solution was then centrifuged to separate the solid product, which was washed repeatedly with methanol and acetone and dried under vacuum. (Yield = 75%)

Method 2. The same procedure was employed by milling a mixture of [PTA-CH$_2$-C$_6$H$_4$-p-COOH]Br (500 mg, 1.34 mmol, 2 equiv.), CuBr (96.1 mg, 0.67 mmol, 1 equiv.) and Zn(OAc)$_2$·2H$_2$O (147 mg, 0.67 mmol, 1 equiv.). (Yield = 64%)

Elemental analysis calcd (%) for $C_{28}H_{36}Br_3CuN_6O_4P_2Zn$: C 35.36, H 3.81, N 8.84; found: C 35.71, H 3.98, N 8.87. ICP calcd (%): Cu 6.68, Zn 6.8; found: Cu 6.74, Zn 6.78. FTIR (KBr): ν (cm^{-1}) = 1687 w, 1605 s, 1559 m, 1457 w, 1367 s, 1306 w, 1206 w, 1178 w, 1116 w, 1093 m, 1013 m, 983 m, 925 m, 900 w, 848 m, 813 m, 771 s, 711 m, 687 m, 649 w, 557 m, 544 m, 427 m. ^{31}P ssNMR (202.5 MHz, δ): br s −76.21. ^{13}C ssNMR (125.8 MHz, δ): 174.8 (COO$^-$), 138.84 (C–Ar), 132.93 (C–Ar), 84.13 (NCH$_2$N$^+$), 78.02 (NCH$_2$N$^+$), 71.33 (NCH$_2$N), 67.1 (CCH$_2$N$^+$), 58.78 (PCH$_2$N$^+$), 49.16 (PCH$_2$N), 42.05 (PCH$_2$N).

([CuBr$_2${PTA-CH$_2$-C$_6$H$_4$-p-COO}$_2$M]Br)$_n$ {M=Ni^{2+} for 4 or Cu^{2+} for 5}

The same procedure for preparing 3 was utilized by milling a mixture of [PTA-CH$_2$-C$_6$H$_4$-p-COOH]Br (500 mg, 1.34 mmol, 2 equiv.), CuBr (96.1 mg, 0.67 mmol, 1 equiv.) and Ni(OAc)$_2$·2H$_2$O (166.7 mg, 0.67 mmol, 1 equiv.) to obtain 4 or Cu(OAc)$_2$·H$_2$O (133.7 mg, 0.67 mmol, 1 equiv.) to obtain 5.

([CuBr$_2${PTA-CH$_2$-C$_6$H$_4$-p-COO}$_2$Ni] Br)$_n$ (4)

Yield = 56%. Elemental analysis calcd (%) for $C_{28}H_{36}Br_3CuN_6NiO_4P_2$: C 35.61, H 3.84, N 8.90; found: C 35.47, H 3.72, N 8.83. ICP calcd (%): Cu 6.73, Ni 6.21; found: Cu 6.55, Ni 6.39. FTIR (KBr): ν (cm^{-1}) = 1688 m, 1608 m, 1544 m, 1454 w, 1399 s, 1306 m, 1250 w, 1215 m, 1174 w, 1118 s, 1098 m, 1069 s, 1034 s, 1011 m, 986 s, 925 m, 903 m, 859 m, 813 s, 761 s, 735 s, 708 w, 687 w, 644 m, 583 w, 554 s, 495 m, 441 s. ^{31}P ssNMR (202.5 MHz, δ): −80.4 (q, $^1J_{cu-P}$ = 1037 Hz). ^{13}C ssNMR (125.8 MHz, δ): 173.63 (COO), 137.11 (C_{quat}–CH$_2$), 136.13 (CH–C–CH$_2$), 132.73 (C_{quat}–COO), 130.01 (CH–C–COO), 84.10 (NCH$_2$N$^+$), 80.21(NCH$_2$N$^+$), 73.48 (NCH$_2$N), 65.94 (CCH$_2$N$^+$), 55.89 (PCH$_2$N$^+$), 51.52 (PCH$_2$N$^+$), 50.32 (PCH$_2$N).

([CuBr{PTA-CH$_2$-C$_6$H$_4$-p-COO}]$_2$Br)$_n$ (5)

Yield = 91%. Elemental analysis calcd (%) for $C_{28}H_{36}Br_3Cu_2N_6O_4P_2$: C 35.42, H 3.82, N 8.85; found: C 35.27, H 3.87, N 8.90. ICP calcd (%): Cu 13.39; found: Cu 13.18. FTIR (KBr): ν (cm^{-1}) = 1703 s, 1617 s, 1544 m, 1509 w, 1448 m, 1403 s, 1305 m, 1250 m, 1208 m, 1180 m, 1117 s, 1066 s, 1031 m, 972 m, 925 m, 902 w, 884 w, 849 m, 812 s, 761 m, 734 s, 688 m, 654 w, 626 w, 589 m, 553 s, 504 s, 441 m.

Preparation of Cu-M@C composites

The pyrolysis of HMOPFs (1 g) was carried out in an inert atmosphere (N_2) in a tube furnace with a heating rate of 5 °C min^{-1}. After annealing 3–5 at 800 °C for 30 minutes, the cooling process to the ambient temperature was carried out at 5 °C min^{-1} rate under N_2 atmosphere, to obtain black solid materials, denoted as Cu–Zn@C (0.41 g), Cu–Ni@C (0.38 g) and Cu–Cu@C (0.44 g), respectively.

Batteries & Supercaps

Research Article
doi.org/10.1002/batt.202300564

Chemistry Europe
European Chemical
Societies Publishing

Fabrication of the electrodes

For the electrochemical measurement studies the powdered NPs were processed to produce an electrode. To that end, an ink was prepared using a standard composition reported elsewhere,[60] that is by mixing 80% of the active material (Cu–M@C composites) with 15% of conducting agent (carbon black), and 5% of the binder polyvinylidene difluoride (PVDF) dispersed in 6 drops of N-methyl-2-pyrrolidone (NMP). The mixture was coated on Toray Carbon Paper®, used as substrate, and dried at 50 °C for 12 h.

Electrochemical Measurement

The electrochemical performance of the electrode material was tested by CV (at scan rates of 10, 15, 20, 25, 30, 40 and 50 mV s^{-1}), GCD curves at different specific currents (2, 3, 5, 8, 10, 15 and 20 A g^{-1}). The cyclic stability was assessed in a 2000 consecutive charge-discharge test. A potentiostat Gamry Instruments Reference 3000 was used for the electrochemical tests which were investigated in 2 M KOH electrolyte using a three-electrode cell configuration. The calomel electrode (SCE) served as reference electrode, Pt spiral as counter electrode, and the coated carbon paper (with NPs) as working electrode. The formula related to the electrochemical parameters are as follows:[61,62]

Mass specific capacitance:

$$C_m = \frac{I \Delta t}{m \, \Delta V} \tag{1}$$

where I represents the charge and discharge current (A), Δt is discharge time (s), I/m is the discharge current density (A g^{-1}), m is the mass loading (g), and ΔV is the voltage window (V) during the charge and discharge process.

Conclusions

In summary, we have developed a new, efficient and eco-friendly HMOPF-derived strategy for the fabrication of bimetallic nanoparticles of transition metal phosphide and phosphate embedded in multi-P,N,Br-codoped carbon matrices (Cu–M@C). The HMOPFs that contain soft/hard metal centres, namely Cu(I)/Zn(II) (**3**), Cu(I)/Ni(II) (**4**) and Cu(I)/Cu(II) (**5**), were obtained using a novel solvent-free mechanochemical approach by reacting an organophosphine linker (PTA-CH$_2$-C$_6$H$_4$-p-COOH)Br with the corresponding metal precursors in a ball mill. The obtained HMOPFs were characterized with solid-state NMR (^{13}C and ^{31}P), IR, elemental analysis and ICP, and their morphologies were investigated using SEM equipped with EDS, and TEM. In the absence of additional P source and Br$_2$ vapour, the Cu–M@C nanocomposites, codoped in P, N and Br were obtained from the corresponding HMOPF via simple pyrolysis at 800 °C, under N$_2$ atmosphere, avoiding the release of the PH$_3$ gas. The XRD patterns of the Cu–M@C nanocomposites revealed the presence of multi-transition metal phosphide and phosphate phases. Their morphologies and NPs formation were assessed using SEM. The EDS study revealed the highly uniform distribution of the bimetallic transition metal alloy NPs in the multi-P,N,Br-codoped carbon matrices. TEM images exhibited the formation of NPs with diameters lower than 50 nm. XPS attests the formation of zinc pyrophosphate at the Cu–Zn@C composite surface. The Cu(II) oxide

detected by XPS indicates that this oxide is mainly at the nanoparticles outermost surface, while copper phosphide (Cu$_3$P), which is detected by XRD, is at larger depths than CuO, beyond the XPS probing layer. Nitrogen is also detected by XPS, showing a very different spectral profile from the N 1s obtained for the PTA-based organophosphine linker used to synthesise the HMOPFs.[31] Nitrogen is under the form of —N═, >NH and graphitic nitrogen, clearly attesting the doping of the carbon matrix. Some nitrate groups are also present. Bromine is detected by XPS, but in residual amounts. The fact that it is detected by EDS is compatible with bromine being beyond the XPS probing depth.

As a result, the Cu–Zn@C electrode (1.25 V) showed higher potential window than the Cu–Ni@C electrode (0.7 V) and Cu–Cu@C (0.9 V) electrode and achieved a good rate performance of 60% and high coulombic efficiency. Therefore, this study makes this material an interesting candidate as negative electrode for asymmetric supercapacitor assemblies.

The N-alkylated PTA compounds possess rich coordination modes, high coordination selectivity and have been demonstrated to be suitable for obtaining heterometallic complexes, as shown in this study. Therefore, HMOPFs based on those ligands are expected to offer a promising molecular platform for designing diverse heteroatom-doped binary TMPs@C. We are currently exploring the potential of synthesizing HMOPFs with several PTA-core ligands via solvothermal and mechanochemical routes as templates to produce heteroatom-doped binary TMPs@C, which can serve as catalysts and energy storage materials. Although the pyrolysis of HMOPFs presented in this study did not lead to the formation of binary TMPs (M^1_xM^2_yP) as a result of an elemental alloying process, we are exploring modifications to the organophosphine linker structures and pyrolysis conditions to pursue this goal.

Conflict of Interests

The authors declare no conflict of interest.

Data Availability Statement

The data that support the findings of this study are available in the supplementary material of this article.

[1] D. Larcher, J. M. Tarascon, *Nat. Chem. 2014 71* **2014**, *7*, 19–29.
[2] C. Liedel, *ChemSusChem.* **2020**, *13*, 2110–2141.
[3] S. Cao, H. Zhang, Y. Zhao, Y. Zhao, *eScience* **2021**, *1*, 28–43.
[4] Z. Li, Y. Zheng, Q. Liu, Y. Wang, D. Wang, Z. Li, P. Zheng, Z. Liu, *J. Mater. Chem. A.* **2020**, *8*, 19113–19132.
[5] Q. Li, D. Yang, H. Chen, X. Lv, Y. Jiang, Y. Feng, X. Rui, Y. Yu, *SusMat.* **2021**, *1*, 359–392.
[6] Q. Zong, C. Liu, H. Yang, Q. Zhang, G. Cao, *Nano Today* **2021**, *38*, 101201.
[7] S. Shi, C. Sun, X. Yin, L. Shen, Q. Shi, K. Zhao, Y. Zhao, J. Zhang, S. S. Shi, Y. F. Zhao, X. P. Yin, L. Y. Shen, Q. H. Shi, K. N. Zhao, J. J. Zhang, C. L. Sun, *Adv. Funct. Mater.* **2020**, *30*, 1909283.
[8] L. M. Cao, J. Zhang, L. W. Ding, Z. Y. Du, C. T. He, *J. Energy Chem.* **2022**, *68*, 494–520.
[9] C. Shuai, Z. Mo, X. Niu, P. Zhao, Q. Dong, Y. Chen, N. Liu, R. Guo, *J. Alloys Compd.* **2020**, *847*, 156514.
[10] Y. Yin, Y. Zhang, N. Liu, L. Fan, N. Zhang, *Energy Environ. Mater.* **2020**, *3*, 529–534.
[11] Y. X. Yang, K. K. Ge, S. Ur Rehman, H. Bi, *Rare Met. 2022 4112* **2022**, *41*, 3957–3975.
[12] C. Wang, B. Yan, J. Zheng, L. Feng, Z. Chen, Q. Zhang, T. Liao, J. Chen, S. Jiang, C. Du, S. He, *Adv. Powder Mater.* **2022**, *1*, 100018.
[13] R. Wang, X. Y. Dong, J. Du, J. Y. Zhao, S. Q. Zang, *Adv. Mater.* **2018**, *30*, 1703711.
[14] M. Sarabaegi, M. Roushani, H. Hosseini, S. Abbasi, *Surfaces and Interfaces* **2021**, *25*, 101207.
[15] M. Kong, H. Song, J. Zhou, *Adv. Energy Mater.* **2018**, *8*, 1801489.
[16] Y. Li, M. Kong, J. Hu, J. Zhou, *Adv. Energy Mater.* **2020**, *10*, 2000400.
[17] X. Wang, L. Chai, J. Ding, L. Zhong, Y. Du, T. T. Li, Y. Hu, J. Qian, S. Huang, *Nano Energy* **2019**, *62*, 745–753.
[18] K. Li, P. Li, Z. Sun, J. Shi, M. Huang, J. Chen, S. Liu, Z. Shi, H. Wang, *Green Energy & Environ.* **2023**, *8*, 1091–1101.
[19] A. Guerriero, M. Peruzzini, L. Gonsalvi, *Coord. Chem. Rev.* **2018**, *355*, 328–361.
[20] A. G. Mahmoud, M. F. C. Guedes da Silva, A. J. L. Pombeiro, *Coord. Chem. Rev.* **2021**, *429*, 213614.
[21] A. G. Mahmoud, M. F. C. Guedes da Silva, P. Smoleński, *in Synth. AndCatalysis Sustain.* (Ed.: A. J. L. Pombeiro), World Scientific Publishing Company, **2024**, pp. 77–106.
[22] A. G. Mahmoud, M. F. C. Guedes da Silva, E. I. Śliwa, P. Smoleński, M. L. Kuznetsov, A. J. L. Pombeiro, *Chem. Asian J.* **2018**, *13*, 2868–2880.
[23] A. G. Mahmoud, P. Smoleński, M. F. C. Guedes Da Silva, A. J. L. Pombeiro, *Molecules* **2020**, *25*, 5479.
[24] A. G. Mahmoud, M. F. C. Guedes da Silva, J. Sokolnicki, P. Smoleński, A. J. L. Pombeiro, *Dalton Trans.* **2018**, *47*, 7290–7299.
[25] A. G. Mahmoud, M. F. C. Guedes da Silva, A. J. L. Pombeiro, *Dalton Trans.* **2021**, *50*, 6109–6125.
[26] I. L. Librando, A. G. Mahmoud, S. A. C. Carabineiro, M. F. C. Guedes da Silva, C. F. G. C. Geraldes, A. J. L. Pombeiro, *Catalysts* **2021**, *11*, 185.
[27] I. L. Librando, A. G. Mahmoud, S. A. C. Carabineiro, M. F. C. Guedes da Silva, C. F. G. C. Geraldes, A. J. L. Pombeiro, *Nanomaterials* **2021**, *11*, 2702.
[28] A. G. Mahmoud, M. F. C. Guedes da Silva, A. J. L. Pombeiro, *Catal. Today* **2023**, *418*, 114056.
[29] D. J. Darensbourg, C. G. Ortiz, J. W. Kamplain, *Organometallics* **2004**, *23*, 1747–1754.
[30] I. L. Librando, A. Paul, A. G. Mahmoud, A. V Gurbanov, S. A. C. Carabineiro, F. C. Guedes da Silva, C. F. G. C. Geraldes, A. J. L. Pombeiro, *RSC Sustain.* **2023**, *1*, 147–158.
[31] A. G. Mahmoud, I. L. Librando, A. Paul, S. A. C. Carabineiro, A. M. Ferraria, A. M. Botelho do Rego, M. F. C. Guedes da Silva, C. F. G. C. Geraldes, A. J. L. Pombeiro, *Catal. Today* **2023**, *423*, 114270.
[32] Z. Liang, C. Qu, W. Zhou, R. Zhao, H. Zhang, B. Zhu, W. Guo, W. Meng, Y. Wu, W. Aftab, Q. Wang, R. Zou, Z. Liang, C. Qu, W. Zhou, R. Zhao, H. Zhang, B. Zhu, W. Guo, W. Meng, Y. Wu, W. Aftab, Q. Wang, R. Zou, *Adv. Sci.* **2019**, *6*, 1802005.
[33] S. Li, R. Wang, X. Yang, J. Wu, H. Meng, H. Xu, Z. Ren, *ACS Sustainable Chem. Eng.* **2019**, *7*, 11872–11884.
[34] J. Du, F. Zhang, Z. Wang, Y. Shang, L. Zhou, Y. Fan, M. Yu, Y. Wang, D. J. Kang, *Mater. Today Commun.* **2020**, *25*, 101257.
[35] H. Chen, Y. Liu, B. Liu, M. Yang, H. Li, H. Chen, *Nanoscale* **2022**, *14*, 12431–12436.
[36] J. Huang, J. Wei, Y. Xiao, Y. Xu, Y. Xiao, Y. Wang, L. Tan, K. Yuan, Y. Chen, *ACS Nano* **2018**, *12*, 3030–3041.
[37] L. Kong, Y. Li, W. Feng, *Trans. Tianjin Univ.* **2022**, *28*, 123–131.
[38] Y. V. Fedoseeva, E. V. Shlyakhova, S. G. Stolyarova, A. A. Vorfolomeeva, M. A. Grebenkina, A. A. Makarova, Y. V. Shubin, A. V. Okotrub, L. G. Bulusheva, *Batteries* **2022**, *8*, 114.
[39] N. Reis Conceição, A. G. Mahmoud, M. F. C. Guedes da Silva, K. T. Mahmudov, A. J. L. Pombeiro, *J. Mol. Catal.* **2023**, *549*, 113512.
[40] G. A. Bowmaker, B. W. Skelton, A. H. White, P. C. Healy, *J. Chem. Soc. Dalton Trans.* **1988**, 2825–2830.
[41] G. A. Bowmaker, S. E. Boyd, J. V. Hanna, R. D. Hart, P. C. Healy, B. W. Skelton, A. H. White, *J. Chem. Soc. Dalton Trans.* **2002**, *13*, 2722–2730.
[42] J. A. Tang, B. D. Ellis, T. H. Warren, J. V. Hanna, C. L. B. Macdonald, R. W. Schurko, *J. Am. Chem. Soc.* **2007**, *129*, 13049–13065.
[43] O. Olofsson, *Acta Chem. Scand.* **1972**, *26*, 2777–2787.
[44] B. E. Robertson, C. Calvo, *J. Solid State Chem.* **1970**, *1*, 120–133.
[45] H. Nowotny, E. Henglein, *Zeitschrift fuer Phys. Chemie, Abteilung B Chemie der Elem. Aufbau der Mater.* **1938**, *40*, 281–284.
[46] H. Effenberger, *Acta Crystallogr. Sect. C* **1990**, *46*, 691–692.
[47] G. L. Shoemaker, J. B. Anderson, E. Kostiner, *IUCr, urn:issn:0567–7408* **1977**, *33*, 2969–2972.
[48] B. E. Robertson, C. Calvo, *Can. J. Chem.* **1968**, *46*, 605–612.
[49] E. Tatarova, A. Dias, J. Henriques, M. Abrashev, N. Bundaleska, E. Kovacevic, N. Bundaleski, U. Cvelbar, E. Valcheva, B. Arnaudov, A. M. B. Do Rego, A. M. Ferraria, J. Berndt, E. Felizardo, O. M. N. D. Teodoro, T. Strunskus, L. L. Alves, B. Gonçalves, *Sci. Rep.* **2017**, *7*, 1–16.
[50] A. V. Naumkin, A. Kraut-Vass, S. W. Gaarenstroom, C. J. Powell, *NIST X-Ray Photoelectron Spectroscopy (XPS) Database, NIST Standard Reference Database 20,* Version 4.1, **2012**.
[51] M. T. Marques, A. M. Ferraria, J. B. Correia, A. M. B. do Rego, R. Vilar, *Mater. Chem. Phys.* **2008**, *109*, 174–180.
[52] Y. C. Chen, Z. B. Chen, Y. G. Lin, Y. K. Hsu, *ACS Sustainable Chem. Eng.* **2017**, *5*, 3863–3870.
[53] P. K. Katkar, S. J. Marje, S. S. Pujari, S. A. Khalate, A. C. Lokhande, U. M. Patil, *ACS Sustainable Chem. Eng.* **2019**, *7*, 11205–11218.
[54] N. Zhang, J. Xu, B. Wei, J. Li, I. Amorim, R. Thomas, S. M. Thalluri, Z. Wang, W. Zhou, S. Xie, L. Liu, *ACS Appl. Energ. Mater.* **2020**, *3*, 4580–4588.
[55] B. Liang, Z. Zheng, M. Retana, K. Lu, T. Wood, Y. Ai, X. Zu, W. Zhou, *Nanotechnology* **2019**, *30*, 295401.
[56] Z. Andikaey, A. A. Ensafi, B. Rezaei, *Electrochim. Acta* **2021**, *393*, 139061.
[57] E. Atrián-Blasco, S. Gascón, M. J. Rodríguez-Yoldi, M. Laguna, E. Cerrada, *Eur. J. Inorg. Chem.* **2016**, *2016*, 2791–2803.
[58] W. T. Dixon, J. Schaefer, M. D. Sefcik, E. O. Stejskal, R. A. McKay, *J. Magn. Reson.* **1982**, *49*, 341–345.
[59] K. Schmidt-Rohr, H. W. Spiess, Eds, *in Multidimens. Solid-State NMR Polym.* Academic Press, London, n,d, p. 110, **1994**.
[60] A. Gören, C. M. Costa, M. M. Silva, S. Lanceros-Méndez, *Composites Part B* **2015**, *83*, 333–345.
[61] L. Xu, L. Zhang, B. Cheng, J. Yu, A. A. Al-Ghamdi, S. Wageh, *J. Mater. Sci. Technol.* **2021**, *78*, 100–109.
[62] X. Zhou, X. Yue, Y. Dong, Q. Zheng, D. Lin, X. Du, G. Qu, *J. Colloid Interface Sci.* **2021**, *599*, 68–78.